

Semiclassical analysis of ellipticity dependence of harmonic yield in graphene

Yongkang Feng ^{1,2,3} Shaoxi Shi,^{1,2,3} Jinbin Li,^{1,2,3} Yajuan Ren,^{1,2,3} Xiao Zhang ^{4,*}
Jianhong Chen,⁵ and Hongchuan Du ^{1,2,3,†}

¹Frontiers Science Center for Rare Isotopes, Lanzhou University, Lanzhou 730000, China

²School of Nuclear Science and Technology, Lanzhou University, Lanzhou 730000, China

³Key Laboratory of Special Function Materials and Structure Design, Ministry of Education, Lanzhou University, Lanzhou 730000, China

⁴School of Physical Science and Technology and Key Laboratory for Magnetism and Magnetic Materials of the MoE, Lanzhou University, Lanzhou 730000, China

⁵School of Electronic and Information Engineering, Lanzhou City University, Lanzhou 730000, China



(Received 29 December 2020; accepted 20 October 2021; published 28 October 2021)

We theoretically investigate the ellipticity dependence of high-order harmonic generation in graphene driven by the midinfrared laser field. The ellipticity dependence of the harmonic yield in the experiment [N. Yoshikawa, T. Tamaya, and K. Tanaka, *Science* **356**, 736 (2017)] is reproduced perfectly by solving the semiconductor Bloch equations in the Houston basis under the tight-binding approximation. Based on the semiclassical recollision model, it is found that the recollision distance of the electron-hole pair excited from the zone $0.5\omega_0 \leq \Delta E \leq 2.5\omega_0$ instead of the Dirac points can reach a minimum value at finite ellipticity, which enhances the harmonic yield. In addition, the ellipticity dependence of harmonics can be controlled by varying the chemical potential of graphene. When the chemical potential is decreased to -1.52 eV, the ellipticity dependence of harmonics can transit into the normal behavior. This work uncovers the microscopic mechanism of the ellipticity dependence of the harmonics in graphene and constructs a clear physical picture to understand the unique ellipticity-dependent behaviors in graphene.

DOI: [10.1103/PhysRevA.104.043525](https://doi.org/10.1103/PhysRevA.104.043525)

I. INTRODUCTION

High-order harmonic generation (HHG) is an important nonperturbative and nonlinear phenomenon in the interaction of intense lasers and matters, which has attracted considerable attention over the past three decades because of its wide applications, such as generating coherent soft x rays [1–3], molecular orbital tomography [4,5], extracting the ionization time [6,7], and probing nuclear dynamics [8–10]. In contrast to gas media, since the first discovery of HHG in ZnO by Ghimire *et al.* [11], many novel phenomena have been gradually observed in solids, such as multiplateaus [12–14], linear scaling of cutoff energy with laser field amplitude [11], and complex orientation dependence [15]. Besides, HHG in solids has been successfully applied to reconstruct the band structure [16–20], measure the Berry curvature [21], extract nonlinear susceptibilities from sapphire [22], image valence electrons at the picometer scale [23], etc.

As the ellipticity dependence of HHG in gases plays an indispensable role in confirming the recollision mechanism and producing isolated attosecond pulses [24–28], the ellipticity dependence of HHG in solids has also been extensively investigated and shows many rich and anomalous behaviors. For example, the harmonic yield of ZnO is suppressed monotonously with increasing ellipticity [11,29]. In rare-gas solids [30] and monolayer MoS₂ [31,32], both of them exhibit an atomiclike ellipticity dependence. However, a later work on

MgO [15,33] shows that the ellipticity profiles are strongly dependent on the angle of polarization. For semimetal graphene, the anomalous ellipticity dependence is also observed that the harmonic yield reaches a maximum at finite ellipticity [32,34]. The complex behavior of ellipticity dependence of solid HHG blocks the further application of polarization gating and double optical gating techniques in solids.

Although the more diverse and anomalous ellipticity-dependent behavior of HHG in solids has attracted much attention, the intrinsic mechanism is still controversial. In MgO, You *et al.* [15] attributed the anomalous ellipticity dependence of HHG to the anisotropy of crystal. However, numerical calculations based on time-dependent density-functional theory [33] indicated that the anomalous ellipticity dependence in MgO results from the intricate nonlinear coupling between the intraband and interband dynamics. In our recent work on ZnO, we found that the recollision of electron-hole pairs dominates the ellipticity dependence of HHG and the ellipticity dependence can transit from atomlike (or normal) to anomalous cases when the vector potential of driving lasers is strong enough [35]. For graphene, the vortex structure of the transition dipole around Dirac points is considered to be responsible for the anomalous ellipticity dependence [34], while Sato *et al.* argued that the anomalous ellipticity dependence in graphene originates from the nonlinear coupling between the intraband and interband transitions [36]. In addition, it has been provided in Ref. [34] that HHG from graphene is mainly contributed by interband currents. This indicates that the electron-hole recollision may play an important role in the anomalous ellipticity dependence in graphene.

*zhangxiao16@lzu.edu.cn

†duhch@lzu.edu.cn

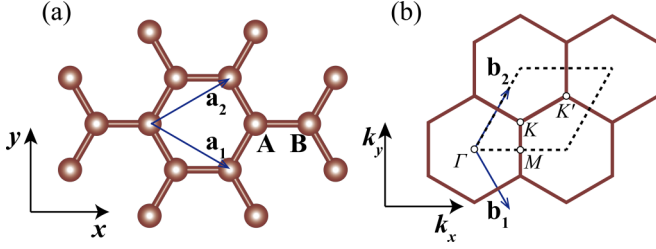


FIG. 1. (a) Hexagonal lattice structure of 2D graphene. (b) Corresponding Brillouin zone in the reciprocal lattice. The diamond-shaped region is equivalent with the first Brillouin zone in area.

In this work, we explore the cause of the anomalous ellipticity dependence of graphene using the recollision model. It is found that the electrons excited from the zone $0.5\omega_0 \leq \Delta E \leq 2.5\omega_0$ around the Dirac point mainly contribute to the HHG at finite ellipticity. Then an intuitive physical picture is established to understand the anomalous ellipticity dependence of graphene. Finally, we propose a practical scheme to control the ellipticity dependence of harmonics generation in graphene.

This paper is organized as follows: In Sec. II, we introduce our theoretical method. In Sec. III, the ellipticity dependence of HHG in graphene is discussed in detail. We reproduce the ellipticity dependence observed in Ref. [32] and discuss the contributions of intraband and interband harmonics to the ellipticity dependence in Sec. III A. Based on the recollision model, the contributions of electrons from different excitation zones to harmonics and the relation between the harmonic yield and recollision distance are discussed in Sec. III B. In Sec. III C, we present a physical picture of the electron-hole dynamics to account for the ellipticity dependence in graphene. In Sec. III D, we show that the ellipticity dependence of HHG in graphene can be controlled by adjusting the chemical potential. Finally, a summary is given in Sec. IV.

II. THEORETICAL METHOD

Graphene is composed of carbon atoms closely packed into a single-layer two-dimensional (2D) honeycomb lattice structure, as shown in Fig. 1(a), where sites A and B denote the two inequivalent atoms in a unit cell. $\mathbf{a}_1 = (\sqrt{3}a/2, a/2)$ and $\mathbf{a}_2 = (\sqrt{3}a/2, -a/2)$ are the two primitive lattice vectors with the lattice constant $a = 2.46 \text{ \AA}$. The corresponding Brillouin zone (BZ) is shown in Fig. 1(b), where $\mathbf{b}_1 = (2\pi/\sqrt{3}a, 2\pi/a)$ and $\mathbf{b}_2 = (2\pi/\sqrt{3}a, -2\pi/a)$ are the reciprocal lattice vectors, and $K = (2\pi/\sqrt{3}a, 2\pi/3a)$ and $K' = (4\pi/\sqrt{3}a, 4\pi/3a)$ are the two inequivalent Dirac points. Since the band structure around the Dirac points varies drastically, we adopt 1000×1000 grids in the diamond-shaped region, shown as the dashed lines in Fig. 1(b).

The electronic structure of graphene is modeled by the tight-binding approximation using π -electron states on the two sublattices as basis functions. The reduced Hamiltonian [37] in reciprocal space can be written as

$$H_0 = \begin{pmatrix} 0 & -\gamma f(\mathbf{k}) \\ -\gamma f^*(\mathbf{k}) & 0 \end{pmatrix}, \quad (1)$$

where the nearest-neighbor hopping γ equals 3.03 eV and the structure factor $f(\mathbf{k})$ is given by

$$f(\mathbf{k}) = \exp\left(i\frac{ak_x}{\sqrt{3}}\right) + 2 \exp\left(-i\frac{ak_x}{2\sqrt{3}}\right) \cos\left(\frac{ak_y}{2}\right). \quad (2)$$

By diagonalizing the Hamiltonian, one can obtain the band structure of the valence and conduction bands $E_{c(v)}(\mathbf{k}) = \pm\gamma|f(\mathbf{k})|$. The corresponding energy eigenvectors are

$$|n\rangle = \frac{1}{\sqrt{2}} \begin{pmatrix} 1 \\ \pm e^{-i\phi(\mathbf{k})} \end{pmatrix}, \quad (3)$$

where n labels the states in the valence (v) and conduction (c) bands, and $\phi(\mathbf{k}) = \text{Arg}[f(\mathbf{k})]$ is the phase of $f(\mathbf{k})$. The negative and positive signs correspond to the valence band and the conduction band, respectively. The interaction of lasers and graphene is described by solving the semiconductor Bloch equations (SBEs) in the Houston representation with the velocity gauge [34,38–40] (atomic units are used throughout unless otherwise stated):

$$i\frac{\partial}{\partial t}\rho_{nm}^{\mathbf{k}(t)} = \left[E_m^{\mathbf{k}(t)} - E_n^{\mathbf{k}(t)} - \frac{i(1 - \delta_{nm})}{T_2} \right] \rho_{nm}^{\mathbf{k}(t)} - \mathbf{E}(t) \cdot \sum_{m'} [\mathbf{d}_{m'n}^{\mathbf{k}(t)} \rho_{m'm}^{\mathbf{k}(t)} - \mathbf{d}_{mm'}^{\mathbf{k}(t)} \rho_{nm'}^{\mathbf{k}(t)}]. \quad (4)$$

Here $\rho_{nm}^{\mathbf{k}(t)}$ is the density matrix element between the m band and n band. $E_m^{\mathbf{k}(t)}$ is the energy of the m band and T_2 is the decoherence time. The $\mathbf{d}_{nm}^{\mathbf{k}(t)}$ denotes the dipole matrix element, which is calculated by

$$\mathbf{d}_{nm}^{\mathbf{k}(t)} = i\langle u_n^{\mathbf{k}(t)} | \nabla_{\mathbf{k}} | u_m^{\mathbf{k}(t)} \rangle. \quad (5)$$

The electric field $\mathbf{E}(t)$ of the laser is given by

$$E_x(t) = \frac{1}{\sqrt{1 + \varepsilon^2}} E_0 f(t) \cos(\omega_0 t), \\ E_y(t) = \frac{\varepsilon}{\sqrt{1 + \varepsilon^2}} E_0 f(t) \sin(\omega_0 t), \quad (6)$$

where E_0 is the amplitude of the electric field, ε the ellipticity, and ω_0 the angular frequency. $f(t)$ has the form of a \cos^2 envelope. We solve the SBEs by the classical fourth-order Runge-Kutta method with the time step 0.65 a.u. and the results are tested for convergence with respect to the diamond-shaped region, sampling points and time steps. The harmonic spectrum is obtained by the modulus square of the Fourier transform of the electric current. The electric current can be calculated by

$$\mathbf{j}(t) = - \sum_{(m,n) \in (c,v)} \int_{\text{BZ}} \mathbf{p}_{mn}^{\mathbf{k}(t)} \rho_{mn}^{\mathbf{k}(t)} d^2\mathbf{k}, \quad (7)$$

where the $\mathbf{p}_{mn}^{\mathbf{k}(t)}$ is the matrix element of the momentum operator. Further, the intraband and interband currents can be calculated by

$$\mathbf{j}_{ra}(t) = - \sum_{m=c,v} \int_{\text{BZ}} \mathbf{p}_{mm}^{\mathbf{k}(t)} \rho_{mm}^{\mathbf{k}(t)} d^2\mathbf{k}, \quad (8)$$

$$\mathbf{j}_{er}(t) = - \left[\int_{\text{BZ}} \mathbf{p}_{cv}^{\mathbf{k}(t)} \rho_{cv}^{\mathbf{k}(t)} d^2\mathbf{k} + \text{c.c.} \right]. \quad (9)$$

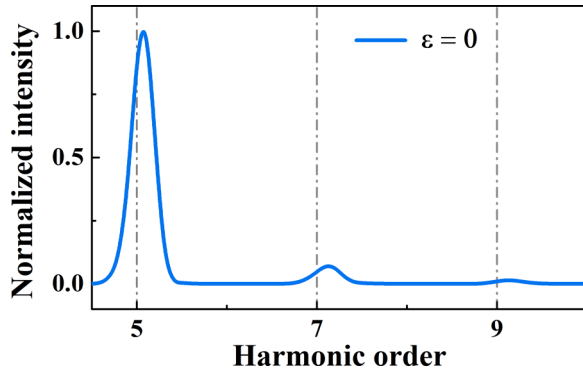


FIG. 2. Harmonic spectrum calculated by the SBEs with the dephasing time $T_2 = 3$ fs in the linearly polarized field ($\varepsilon = 0$).

III. RESULTS AND DISCUSSION

A. Ellipticity dependence of HHG in graphene

First, we calculate the ellipticity dependence of the harmonic yield in graphene. Here, a ten-cycle laser pulse is adopted with the wavelength $\lambda = 4700$ nm ($\omega_0 = 0.26$ eV) (same as the parameter used in Ref. [32]). In order to obtain the minimum difference between calculated and experimental results, we scan the electric field strength E_0 and the decoherence time T_2 , which finally gives $E_0 = 3.6$ MV/cm and $T_2 = 3$ fs. The major polarization axis is set along Γ -M. The high-order harmonic spectrum excited by the linearly polarized pulse is shown in Fig. 2. One can see that the harmonic peaks are clear and discrete. The harmonic intensity decreases significantly with the increasing harmonic order, which is consistent with the experimental results. Besides, we can see that the harmonic peaks are shifted from the expected odd values, as appeared in Refs. [32,34,41]. For this phenomenon, Baudisch *et al.* performed a detailed investigation in Ref. [41].

Figure 3 shows the ellipticity dependence of the seventh harmonic (HH7), where the yield of the n th harmonic is

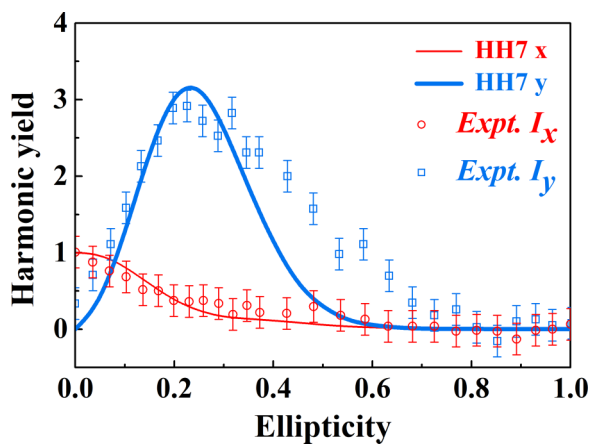


FIG. 3. Ellipticity dependence of harmonics calculated by SBEs, which is separated according to the polarization direction. The circles and squares are the experimental data in Ref. [32]. For comparison, the calculated harmonic yield is normalized to the maximum value of the experimental data.

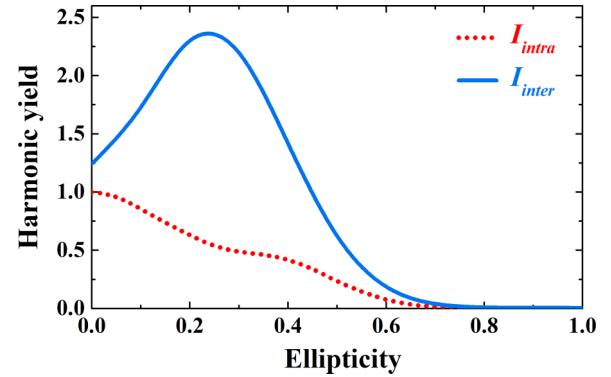


FIG. 4. Ellipticity dependence of seventh harmonic yield calculated by the intraband (red dotted line) and interband (blue curved line) currents. The harmonic yield is normalized to the intraband harmonic yield in $\varepsilon = 0$.

evaluated by

$$I_n = \int_{(n-0.5)\omega_0}^{(n+0.5)\omega_0} I(\omega) d\omega. \quad (10)$$

For comparison, the experimental data [32] are also presented by circles and squares. As shown in Fig. 3, our results reproduce the features of ellipticity dependence of HHG in the experiment [32]. With increasing the ellipticity, the x component (red thin curve) of HH7 yield decreases monotonically, whereas the y component (blue thick curve) reaches the maximum value at around $\varepsilon = 0.25$ and then decreases monotonically. It indicates that the anomalous ellipticity dependence of harmonic yield in graphene results from the microscopic mechanism.

Currently, the intraband and interband harmonics are considered as the two main sources of solid HHG [12,42,43]. Next, we discuss which mechanism dominates the generation of harmonics in graphene. It has been demonstrated in Ref. [32] that the intraband mechanism cannot explain the ellipticity dependence of graphene harmonics. Thus, the interband mechanism may dominate the HHG in graphene. To verify it, we calculate the ellipticity dependence of the interband and intraband harmonics and show the results in Fig. 4. Here, both of the harmonic yields are normalized to the intraband harmonic yield in the linearly polarized laser. We can see that the interband harmonic yield is dominant throughout the whole ellipticity range. The intraband harmonic yield decreases monotonically with the increasing ellipticity while the interband harmonic yield reaches the maximum value at around $\varepsilon = 0.25$ and then decreases monotonically, which is consistent with Fig. 4. Therefore, it indicates that the anomalous ellipticity dependence of the harmonic yield in graphene results from the interband mechanism, in which the electron-hole recollision plays an important role.

B. Semiclassical recollision model

In order to investigate the intrinsic mechanism of anomalous ellipticity dependence in graphene, the electron-hole recollision model is employed. Derived from the SBEs, the

formal solution of interband harmonics is given by

$$J(\omega) = - \int_{BZ} d\mathbf{k} \int_{-\infty}^{\infty} dt \left\{ i [E_c^{\mathbf{k}(t)} - E_v^{\mathbf{k}(t)}] \mathbf{d}_{cv}^{\mathbf{k}(t)} \int_{-\infty}^t dt' \right. \\ \left. \times i \mathbf{E}(t') \cdot \mathbf{d}_{vc}^{\mathbf{k}(t')} (\rho_{vv}^{\mathbf{k}_0} - \rho_{cc}^{\mathbf{k}_0}) e^{i[S(\mathbf{k}_0, t', t) - \omega t]} dt' + \text{c.c.} \right\}, \quad (11)$$

where $\rho_{vv}^{\mathbf{k}_0}$ ($\rho_{cc}^{\mathbf{k}_0}$) is the electron density in the valence (conduction) band, $S(\mathbf{k}_0, t', t) = \int_{t'}^t [E_c^{\mathbf{k}(\tau)} - E_v^{\mathbf{k}(\tau)}] d\tau$ is the classical action, and $\mathbf{k}(\tau) = \mathbf{k}_0 + \mathbf{A}(\tau)$ is the transformed crystal momentum. Owing to the zero-gap property of the Dirac cone structure in graphene, the recollision model must be improved to describe the generation of interband harmonics in graphene. According to Eq. (11) and the condition for the stationary-phase method, the modified saddle-point equations are given by

$$\left| \int_{t'}^t \Delta \mathbf{v}[\mathbf{k} - \mathbf{A}(t) + \mathbf{A}(\tau)] d\tau \right| \leq R_c, \quad (12a)$$

$$E_g[\mathbf{k} - \mathbf{A}(t) + \mathbf{A}(t')] = \Delta E, \quad (12b)$$

$$E_g(\mathbf{k}) - \omega + \mathbf{E}(t) \cdot \Delta \mathbf{r} = 0, \quad (12c)$$

where $\mathbf{k} = \mathbf{k}_0 + \mathbf{A}(t)$, $\Delta \mathbf{r} = \int_{t'}^t \Delta \mathbf{v} d\tau$, $E_g(\mathbf{k}) = E_c^{\mathbf{k}} - E_v^{\mathbf{k}}$, and $\Delta \mathbf{v}(\mathbf{k}) = \nabla_{\mathbf{k}} E_g(\mathbf{k}) = \mathbf{v}_e - \mathbf{v}_h$ is the velocity difference between the electron and the hole. An electron-hole pair is created at the time t' and the initial crystal momentum \mathbf{k}_0 , and they recollide with each other at the recollision time t . R_c is the recollision threshold value and $\Delta \mathbf{r}$ is the relative distance of the electron-hole pair at the recollision time t , which comes from the imperfect recollision [35,44]. When the relative distance between the electron and its associated hole is smaller than R_c , the recollision is taken into account. Based on this condition, the relation between the recollision distance and the harmonic yield can be investigated.

In the unimproved recollision model, Eq. (12b) is usually written as $E_g(\mathbf{k}) = 0$. However, because of the zero-gap property of graphene, contributions of the zone around the Dirac point cannot be ignored (see Refs. [34,45]). Therefore, we consider the area $0 \leq \Delta E \leq 2.5\omega_0$ near the point as the excitation conditions in the improved recollision model. That is, the excitation can happen when the electrons are located in this area. As is known, the probability of electron excitation decreases exponentially as the band gap increases. Moreover, we find that the electron and hole excited from the zone $\Delta E > 2.5\omega_0$ can hardly recollide. Thus, the zone of $\Delta E > 2.5\omega_0$ is not considered in the recollision model. By adjusting ΔE , we can find out which areas mainly contribute to the generation of high-order harmonics. For the Dirac point with zero gap, the solution of Eq. (12b) is real. For the zone with a gap around the Dirac point, we make an approximation and ignore the imaginary part of the solution. This is reasonable because the band gap is very small and the imaginary part is a small value. When the minimum relative distance $\Delta \mathbf{r}$ is less than the threshold value R_c , the recollision takes place and we can obtain the excitation time t' and the recollision time t from Eqs. (12a) and (12b). Then the emitting photon energy is determined using Eq. (12c). In Eq. (12c), we also consider

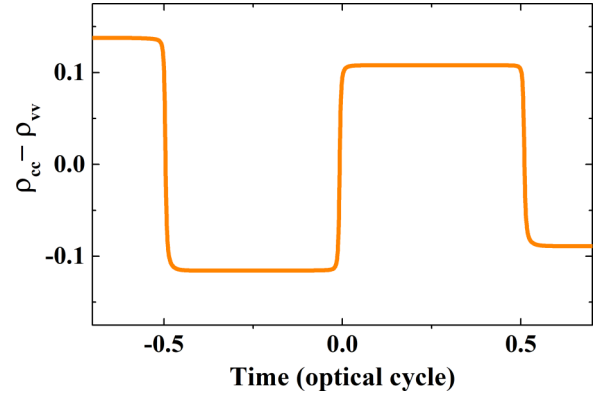


FIG. 5. $\rho_{vv} - \rho_{cc}$ as a function of time at the Dirac point.

the polarization energy of electron-hole pairs owing to the imperfect recollisions [44].

For the gapless system, the interband transitions can take place even with a weak laser field because of the zero-gap property. Thus, it is necessary to clarify whether it is reasonable to apply the stationary-phase method to derive the saddle-point equations in Eq. (12c) from Eq. (11). For this reason, we discuss the population difference $\rho_{vv} - \rho_{cc}$ at the Dirac point in the linearly polarized laser field because it varies most dramatically. Figure 5 shows the variation of $\rho_{vv} - \rho_{cc}$ as a function of time. We can see that the period of $\rho_{vv} - \rho_{cc}$ is one optical cycle (o.c.); $\rho_{vv} - \rho_{cc}$ changes significantly near -0.5 and 0.0 o.c. This is because the electrons undergo the Dirac point in these moments, and they can easily transit between the valence band to the conduction band even with a weak field. Fortunately, $\rho_{vv} - \rho_{cc}$ is constant between the birth and recombination times so that the saddle-point condition can be satisfied well. To verify it, we numerically calculate the following two parts in Eq. (11):

$$\int_{t'}^t (\rho_{vv}^{\mathbf{k}_0} - \rho_{cc}^{\mathbf{k}_0}) e^{iS(\mathbf{k}_0, t', t)} dt, \quad (13a)$$

$$\int_{t'}^t -0.12 e^{iS(\mathbf{k}_0, t', t)} dt, [\rho_{vv}^{\mathbf{k}_0} - \rho_{cc}^{\mathbf{k}_0} = -0.12(\text{const})]. \quad (13b)$$

In the saddle-point approximation, the applicability condition for the stationary-phase method is that the phase in an integrand oscillates much faster than the rest of the integrand. Thus, we set $\rho_{vv}^{\mathbf{k}_0} - \rho_{cc}^{\mathbf{k}_0} = -0.12$ in Eq. (13b), which is obtained from Fig. 5. If the result of Eq. (13a) is consistent with that of Eq. (13b) from the excitation time (t') to the recollision time (t), then the stationary-point approximation is applicable. Figure 6 shows the integration values of the two equations for the seventh harmonic, where the excitation time and recollision time are obtained from the classical trajectory by the recollision model. One can see that both real and imaginary parts of the integration value obtained by the stationary-phase method are the same as the numerical calculations from the excitation time to the recollision time. This indicates that the phase in the integrand oscillates much faster than the rest of the integrand. Besides, similar behavior as the dramatic reversal of the population in Fig. 5 has also been studied in the gas HHG [46,47]. In this case, the classical trajectories are still in good agreement with the time-frequency

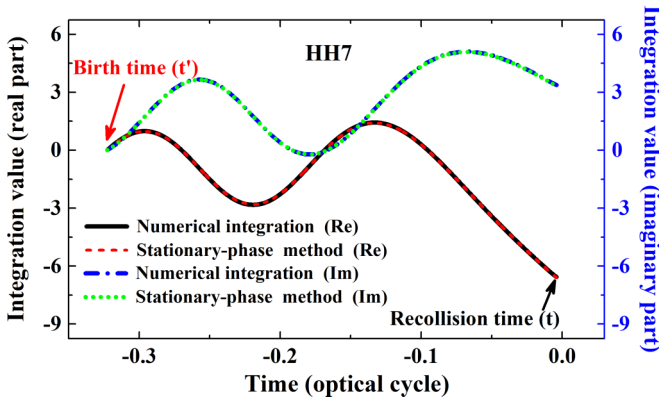


FIG. 6. Integration values of Eqs. (13a) and (13b) for seventh harmonic.

distribution. Therefore, it is reasonable to apply the condition of the stationary-phase method in the saddle-point equations in graphene.

In the following, we discuss the recollision dynamics of HHG from graphene by using the improved recollision model. The case of the linearly polarized laser field is first considered. Figure 7 shows the time-frequency distribution of the harmonics and the corresponding classical trajectories (black dots) calculated by the recollision model, in which the recollision distance is set as 30 a.u. and the excited position (\mathbf{k}_0) is located at the Dirac point. One can see that the classical trajectories are in good agreement with the time-frequency distribution. It is worth mentioning that in addition to the Dirac point, we also consider the contributions of its nearby area by adjusting the value range of ΔE in Eq. (12b). However, it is hard to obtain a recollision trajectory even with a very large recollision distance (60 a.u.). Therefore, the electrons excited at the Dirac point mainly contribute to the HHG of graphene in the driving of the linearly polarized laser pulse. In addition, one can see that the wiggling feature appears around the cutoff in Fig. 7, which is not reproduced by the classical trajectories. This phenomenon comes from the interference between the quantum paths from different excitation zones owing to the weak intensity of the main quantum path near the cutoff.

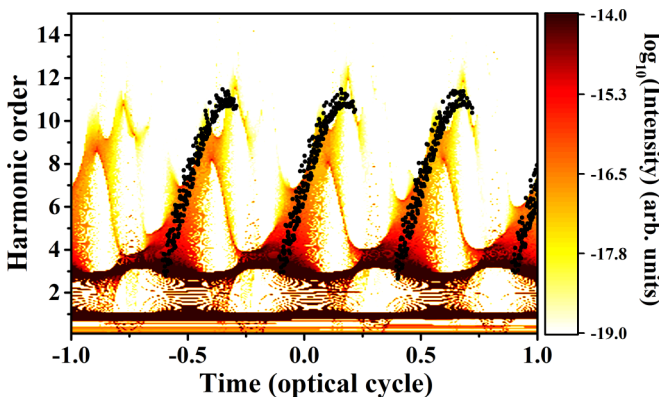


FIG. 7. Time-frequency distribution of the HHG driven by the linearly polarized laser pulse, in which the black dots represent the classical trajectories with the excited condition set as the Dirac point. The recollision distance is set as $R_c = 30$ a.u.

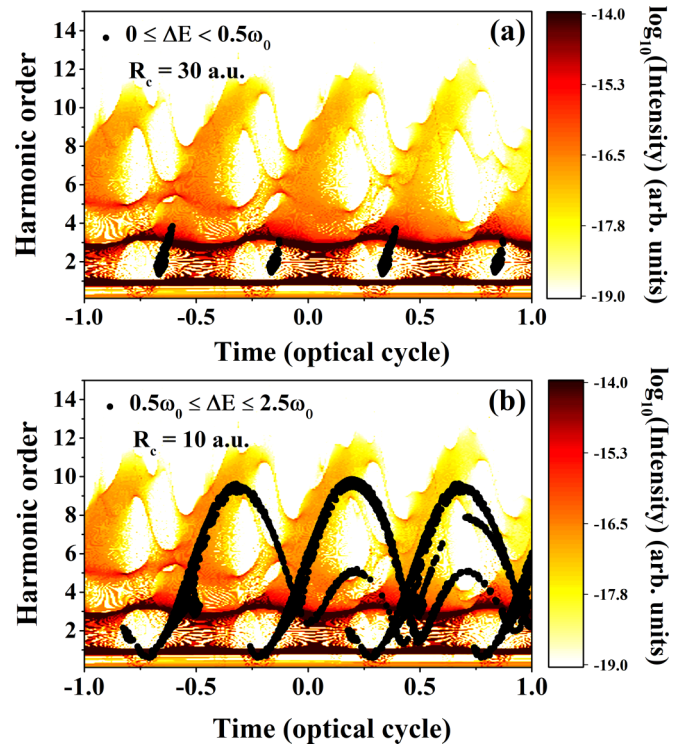


FIG. 8. Time-frequency distribution and the classical trajectories with the driving laser field at $\varepsilon = 0.2$. (a) The excitation condition is set to the area $0 \leq \Delta E \leq 0.5\omega_0$ near the Dirac point and $R_c = 30$ a.u. (b) The excitation area $0.5\omega_0 \leq \Delta E \leq 2.5\omega_0$ and $R_c = 10$ a.u.

Next, we turn to the case of the elliptically polarized laser pulse ($\varepsilon = 0.2$), in which the harmonic yield is near the maximum. Figures 8(a) and 8(b) show the time-frequency distribution of HHG. To analyze the behaviors of the electron-hole pairs, we divide the excitation areas into two parts in the recollision model, i.e., $0 \leq \Delta E < 0.5\omega_0$ and $0.5\omega_0 \leq \Delta E \leq 2.5\omega_0$. The corresponding classical trajectories are presented with black dots in Figs. 8(a) and 8(b). One can find that when the excitation zone is set as $0 \leq \Delta E < 0.5\omega_0$, the classical trajectories survive only from first order to fourth order, which obviously disagrees with the quantum paths. However, when the excited zone is chosen as $0.5\omega_0 \leq \Delta E \leq 2.5\omega_0$, the classical trajectories up to the cutoff energy can still be obtained for a very small recollision distance of $R_c = 10$ a.u. Furthermore, they are in good agreement with the quantum paths. It is worth noting that near the cutoff region, the agreement is rather poor and the time-frequency distribution is at higher orders. This is because the quantum path in this region results from the recollision with larger recollision distances ($25 < R_c < 30$ a.u.). Thus, the electrons excited in the zone $0.5\omega_0 \leq \Delta E < 2.5\omega_0$ mainly contribute to the HHG while the laser ellipticity equals 0.2. The enhancement of the harmonic yield at the ellipticity of $\varepsilon = 0.2$ stems from the smaller recollision distance.

To figure out the relation between the recollision distance and the harmonic yield, we present the minimum recollision distances and the total yield of HH7 at different ellipticities in Fig. 9, where the excited zone is set by $0 \leq \Delta E \leq 2.5\omega_0$. It is obvious that the yield of HH7 is negatively correlated with

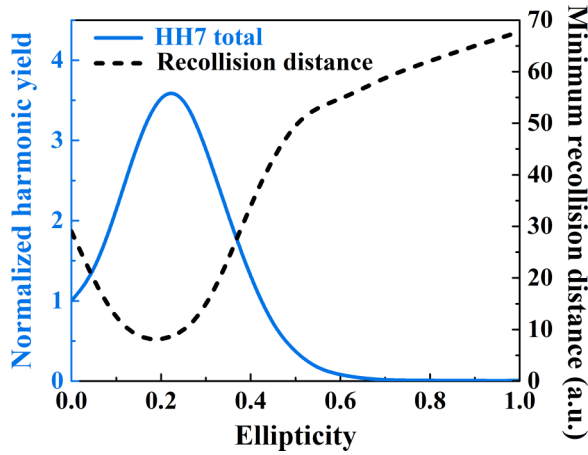


FIG. 9. Normalized total harmonic yield (blue solid line) and the minimum recollision distance of HH7 (black dashed line) as a function of the ellipticity. The excitation zone is set as $0 \leq \Delta E \leq 2.5\omega_0$ in the calculations.

the minimum recollision distance and reaches a maximum when the distance is around its minimum. This proves that the recollision dynamics is still valid for the anomalous ellipticity dependence in graphene.

C. Trajectory analysis

Having confirmed the relation between the harmonic yield and the recollision distance, two questions have not been clarified yet, namely, (i) why the recollision distance first decreases and then increases with the increasing ellipticity and (ii) why the main contribution of excitation area to the HHG is different with the increasing ellipticity.

To answer question (i), we show the real-space trajectories (solid lines) of the electron-hole pairs at different ellipticities in Figs. 10(a)–10(d), where the recollision distances are marked by the blue arrows. For $\varepsilon = 0$, after being created and pulled apart, the electron and hole can reverse in the x direction and recollide at a distance of 29.05 a.u., as shown in Fig. 10(a). However, for $\varepsilon = 0.2$, the electron and hole can reverse in both x and y directions and form an approximately closed trajectory. Finally, the recollision takes place at a distance of 7.49 a.u., emitting a harmonic photon. Such a small recollision distance results in the enhancement of the harmonic yield. As the ellipticity is further increased, the recollision distance gradually increases, leading to the decrease in the recollision probability and the harmonic yield, as shown in Figs. 10(c) and 10(d).

For question (ii), we take the case of $\varepsilon = 0$ as an example and discuss the motion of the electron-hole pairs in detail. The circles and squares in Fig. 10(a) represent the real-space trajectories of electron-hole pairs excited away from the Dirac point. Clearly, electron-hole pairs are pulled apart in the y direction and their distance increases monotonously. Thus, the electron and hole cannot recollide even by setting a vary large recollision distance. To get more insight, we show the distributions of the relative velocity between electrons and holes in the x and y directions in Figs. 11(a) and 11(b), respectively. For the linearly polarized laser pulse ($\varepsilon = 0$),

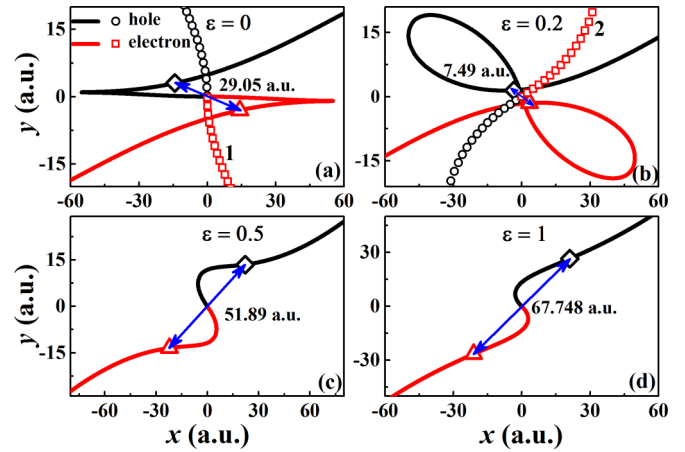


FIG. 10. Real-space trajectories of the electron-hole pair: (a) $\varepsilon = 0$, (b) $\varepsilon = 0.2$, (c) $\varepsilon = 0.5$, and (d) $\varepsilon = 1$. Many recollision events contribute to the seventh harmonic generation, so we pick out the representative trajectories with the smallest recollision distance. The blue arrows represent the recollision distance. Trajectory 1 in (a) denotes the trajectory excited from a position away from the Dirac point, and trajectory 2 in (b) represents the trajectory excited from the Dirac point.

as shown by the black path 1 in Fig. 11(a), the electrons excited away from the Dirac point can move in both the purple and orange regions, which corresponds to the change of the relative velocity from positive to negative. Thus the electron and hole can reverse in the x direction. However, in the y direction, the electrons always keep moving in the purple region and cannot travel into the orange area [see path 1 in Fig. 11(b)]; namely, the relative velocity between the electron and hole in the y direction is negative at all times. Thus the electron and hole cannot reverse in the y direction. Therefore, the electrons excited away from the Dirac point hardly contribute to the generation of harmonics for $\varepsilon = 0$. The similar behavior can also be observed in the electrons excited from the Dirac point at $\varepsilon = 0.2$ (see the blue path 2 in Figs. 10 and 11). In this case, the relative velocity in the y direction is always positive, leading to that the electrons and holes are pulled apart in the y direction. As a result, the electrons excited from the zone $0 \leq \Delta E < 0.5\omega_0$ hardly contribute to the HHG at $\varepsilon = 0.2$. This is the reason that the excitation area that mainly contributes to the HHG is different with increasing the ellipticity.

D. Control of ellipticity dependence of HHG in graphene

After understanding the intrinsic mechanism of the unique ellipticity dependence of harmonic yield in graphene, we further investigate the control for the ellipticity dependence of HHG in graphene. According to our conclusions above, this can be achieved by controlling the excitation. If we remove the electrons in the zone $0.5\omega_0 \leq \Delta E \leq 2.5\omega_0$, the generation of harmonics driven by the elliptically polarized laser may not be enhanced. In graphene, we can suppress the excitation channels around the Dirac points by adjusting the chemical potential. Indeed, varying the chemical potential has been proposed in Ref. [36] to enhance the intensity

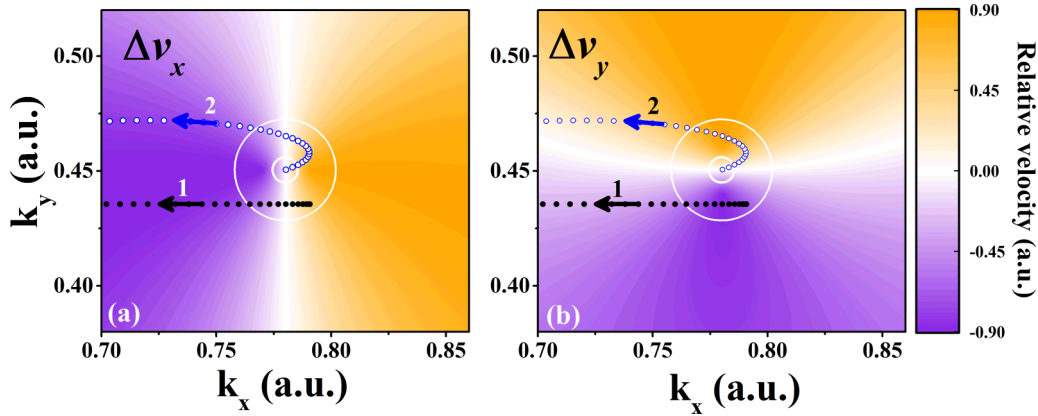


FIG. 11. Distributions of the relative velocity in k space in the (a) x and (b) y directions. The electron trajectories in k space of trajectory 1 in Fig. 10(a) and trajectory 2 in Fig. 10(b). The inner (outer) circle denotes the boundary of $\Delta E = 0.5\omega_0$ ($\Delta E = 2.5\omega_0$).

of the harmonic by canceling the destructive interference. Differently, we focus on another aspect of the harmonic: ellipticity dependence as a function of the chemical potential. In the experiment, the chemical potential can be controlled by gate voltage, electric field, magnetic field, chemical doping [48–51], and so on. In the calculation of the SBEs, the variation of the chemical potential can be achieved by setting the initial diagonal element $\rho_{vv}^k = 1$ below the the Fermi surface, which represents the initial population probability in the valence band. Figure 12(a) shows the Fermi surfaces with the different chemical potentials μ . As the chemical potential decreases, the Fermi surface will decrease and the electrons excited in the zone $0.5\omega_0 \leq \Delta E \leq 2.5\omega_0$ will be gradually reduced. When the chemical potential decreases to -1.06 eV, as shown in Fig. 12(a), some of the electrons are still able to be driven into the zone $0.5\omega_0 \leq \Delta E \leq 2.5\omega_0$ by the laser field. At this point, the major excitation region does not change and the enhancement of harmonic yield at finite ellipticity will be weakened. As the chemical potential further decreases to -1.52 eV, few electrons can be driven into the zone $0.5\omega_0 \leq \Delta E \leq 2.5\omega_0$. Therefore, the major excitation region changes and the enhancement of the harmonic yield will vanish. The anomalous ellipticity dependence will transform to a normal ellipticity dependence. To verify our speculation, Fig. 12(b) shows the ellipticity dependence of HH7 with different chemical potentials μ . It is obvious that the harmonic yield at around $\varepsilon = 0.25$ gradually decreases and eventually transits into the normal ellipticity dependence at $\mu = -1.52$ eV, which is in accordance with our expectations. Besides, it is noted that both increasing and reducing chemical potential are the same in controlling the harmonic generation of graphene due to the electron-hole symmetry in graphene.

IV. CONCLUSION

We investigated the ellipticity dependence of HHG in graphene by solving the SBEs. According to the saddle-point analysis, we found that the excitation area contributing to the HHG is different at different ellipticities. The electrons excited from the zone ($0.5\omega_0 \leq \Delta E \leq 2.5\omega_0$) are mainly responsible for the enhancement of the harmonic yield at

finite ellipticity. In-depth analyses reveal that the motion of the electron and hole from this zone can form a closed trajectory, leading to a minimum recollision distance. Thereby, the harmonic yield is enhanced. Besides, we propose a way to control the ellipticity dependence of HHG in graphene by varying the chemical potential. As the chemical potential decreases, the electrons excited in the zone ($0.5\omega_0 \leq \Delta E \leq 2.5\omega_0$) are gradually reduced. Thus, the enhancement of harmonics at finite ellipticity progressively diminishes.

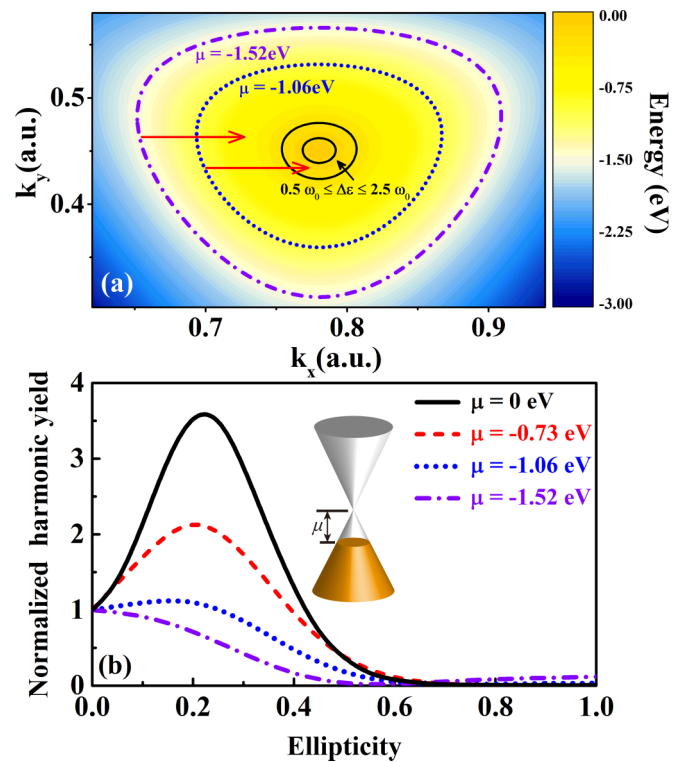


FIG. 12. (a) Top view of the Fermi surfaces at different chemical potentials in the valence band. The red arrow marks the vector potential of the laser field. The black annulus denotes the zone of $0.5\omega_0 \leq \Delta E \leq 2.5\omega_0$. (b) Ellipticity dependence of HH7 at different chemical potentials μ . The inserted figure presents the sketch map of varying the chemical potential.

Eventually, the ellipticity dependence transits to be normal. We expect this shift to be observed in the future experiments. Previous works have presented that the zero-gap property and the vortex structure of the dipole matrix element near the Dirac point play a key role in the anomalous ellipticity dependence [32,34]. Our results further uncover the underlying mechanism and provide a deeper understanding of the anomalous ellipticity dependence in graphene. In addition, this also provides an intuitive physical picture for understanding the ellipticity-dependent behaviors in a variety of materials with the zero-gap band structure, such as three-dimensional

topological insulators, and AA- and AB-stacked bilayer graphene.

ACKNOWLEDGMENTS

This work was supported by the National Natural Science Foundation of China (NSFC) (Grants No. 11874030, No. 11904146, and No. 12064023), the Natural Science Foundation of Gansu Province (Grant No. 20JR5RA209), and the Scientific Research Program of the Higher Education Institutions of Gansu Province of China (Grant No. 2020A-125).

-
- [1] T. Popmintchev, M.-C. Chen, P. Arpin, M. M. Murnane, and H. C. Kapteyn, The attosecond nonlinear optics of bright coherent x-ray generation, *Nat. Photon.* **4**, 822 (2010).
- [2] F. Silva, S. M. Teichmann, S. L. Cousin, M. Hemmer, and J. Biegert, Spatiotemporal isolation of attosecond soft x-ray pulses in the water window, *Nat. Commun.* **6**, 6611 (2015).
- [3] T. T. Luu, M. Garg, S. Y. Kruchinin, A. Moulet, M. T. Hassan, and E. Goulielmakis, Extreme ultraviolet high-harmonic spectroscopy of solids, *Nature (London)* **521**, 498 (2015).
- [4] J. Itatani, J. Levesque, D. Zeidler, H. Niikura, H. Pépin, J. C. Kieffer, P. B. Corkum, and D. M. Villeneuve, Tomographic imaging of molecular orbitals, *Nature (London)* **432**, 867 (2004).
- [5] S. Haessler, J. Caillat, W. Boutu, C. Giovanetti-Teixeira, T. Ruchon, T. Auguste, Z. Diveki, P. Breger, A. Maquet, B. Carré, R. Taïeb, and P. Salières, Attosecond imaging of molecular electronic wavepackets, *Nat. Phys.* **6**, 200 (2010).
- [6] D. Shafir, H. Soifer, B. D. Bruner, M. Dagan, Y. Mairesse, S. Patchkovskii, M. Y. Ivanov, O. Smirnova, and N. Dudovich, Resolving the time when an electron exits a tunnelling barrier, *Nature (London)* **485**, 343 (2012).
- [7] J. Zhao and M. Lein, Determination of Ionization and Tunneling Times in High-Order Harmonic Generation, *Phys. Rev. Lett.* **111**, 043901 (2013).
- [8] S. Baker, J. S. Robinson, C. A. Haworth, H. Teng, R. A. Smith, C. C. Chirilă, M. Lein, J. W. G. Tisch, and J. P. Marangos, Probing proton dynamics in molecules on an attosecond time scale, *Science* **312**, 424 (2006).
- [9] M. Lein, Attosecond Probing of Vibrational Dynamics with High-Harmonic Generation, *Phys. Rev. Lett.* **94**, 053004 (2005).
- [10] L. He, Q. Zhang, P. Lan, W. Cao, X. Zhu, C. Zhai, F. Wang, W. Shi, M. Li, X.-B. Bian, P. Lu, and A. D. Bandrauk, Monitoring ultrafast vibrational dynamics of isotopic molecules with frequency modulation of high-order harmonics, *Nat. Commun.* **9**, 1108 (2018).
- [11] S. Ghimire, A. D. DiChiara, E. Sistrunk, P. Agostini, L. F. DiMauro, and D. A. Reis, Observation of high-order harmonic generation in a bulk crystal, *Nat. Phys.* **7**, 138 (2011).
- [12] M. Wu, S. Ghimire, D. A. Reis, K. J. Schafer, and M. B. Gaarde, High-harmonic generation from Bloch electrons in solids, *Phys. Rev. A* **91**, 043839 (2015).
- [13] T.-Y. Du, Z. Guan, X.-X. Zhou, and X.-B. Bian, Enhanced high-order harmonic generation from periodic potentials in inhomogeneous laser fields, *Phys. Rev. A* **94**, 023419 (2016).
- [14] J.-B. Li, X. Zhang, S.-J. Yue, H.-M. Wu, B.-T. Hu, and H.-C. Du, Enhancement of the second plateau in solid high-order harmonic spectra by the two-color fields, *Opt. Express* **25**, 18603 (2017).
- [15] Y. S. You, D. Reis, and S. Ghimire, Anisotropic high-harmonic generation in bulk crystals, *Nat. Phys.* **13**, 345 (2017).
- [16] G. Vampa, T. J. Hammond, N. Thiré, B. E. Schmidt, F. Légaré, C. R. McDonald, T. Brabec, D. D. Klug, and P. B. Corkum, All-Optical Reconstruction of Crystal Band Structure, *Phys. Rev. Lett.* **115**, 193603 (2015).
- [17] A. A. Lanin, E. A. Stepanov, A. B. Fedotov, and A. M. Zheltikov, Mapping the electron band structure by intraband high-harmonic generation in solids, *Optica* **4**, 516 (2017).
- [18] L. Li, P. Lan, L. He, W. Cao, Q. Zhang, and P. Lu, Determination of Electron Band Structure using Temporal Interferometry, *Phys. Rev. Lett.* **124**, 157403 (2020).
- [19] C. Yu, S. Jiang, T. Wu, G. Yuan, Z. Wang, C. Jin, and R. Lu, Two-dimensional imaging of energy bands from crystal orientation dependent higher-order harmonic spectra in *h*-BN, *Phys. Rev. B* **98**, 085439 (2018).
- [20] L.-J. Lü and X.-B. Bian, Ultrafast intraband electron dynamics of preexcited SiO₂, *Opt. Express* **28**, 13432 (2020).
- [21] T. T. Luu and H. J. Wörner, Measurement of the berry curvature of solids using high-harmonic spectroscopy, *Nat. Commun.* **9**, 916 (2018).
- [22] S. Han, L. Ortmann, H. Kim, Y. W. Kim, T. Oka, A. Chacon, B. Doran, M. Ciappina, M. Lewenstein, S.-W. Kim, S. Kim, and A. S. Landsman, Extraction of higher-order nonlinear electronic response in solids using high harmonic generation, *Nat. Commun.* **10**, 3272 (2019).
- [23] H. Lakhotia, H. Y. Kim, M. Zhan, S. Hu, S. Meng, and E. Goulielmakis, Laser picoscopy of valence electrons in solids, *Nature (London)* **583**, 55 (2020).
- [24] P. M. Paul, E. S. Toma, P. Breger, G. Mullot, F. Augé, P. Balcou, H. G. Muller, and P. Agostini, Observation of a train of attosecond pulses from high harmonic generation, *Science* **292**, 1689 (2001).
- [25] M. Hentschel, R. Kienberger, C. Spielmann, G. A. Reider, N. Milosevic, T. Brabec, P. Corkum, U. Heinzmann, M. Drescher, and F. Krausz, Attosecond metrology, *Nature (London)* **414**, 509 (2001).
- [26] P. B. Corkum, Plasma Perspective on Strong Field Multiphoton Ionization, *Phys. Rev. Lett.* **71**, 1994 (1993).
- [27] K. Zhao, Q. Zhang, M. Chini, Y. Wu, X. Wang, and Z. Chang, Tailoring a 67 attosecond pulse through advantageous phase-mismatch, *Opt. Lett.* **37**, 3891 (2012).

- [28] H. Du, L. Luo, X. Wang, and B. Hu, Isolated attosecond pulse generation from pre-excited medium with a chirped and chirped-free two-color field, *Opt. Express* **20**, 9713 (2012).
- [29] C. Liu, Y. Zheng, Z. Zeng, and R. Li, Effect of elliptical polarization of driving field on high-order-harmonic generation in semiconductor ZnO, *Phys. Rev. A* **93**, 043806 (2016).
- [30] G. Ndabashimiye, S. Ghimire, M. Wu, D. A. Browne, K. J. Schafer, M. B. Gaarde, and D. A. Reis, Solid-state harmonics beyond the atomic limit, *Nature (London)* **534**, 520 (2016).
- [31] H. Liu, Y. Li, Y. S. You, S. Ghimire, T. F. Heinz, and D. A. Reis, High-harmonic generation from an atomically thin semiconductor, *Nat. Phys.* **13**, 262 (2017).
- [32] N. Yoshikawa, T. Tamaya, and K. Tanaka, High-harmonic generation in graphene enhanced by elliptically polarized light excitation, *Science* **356**, 736 (2017).
- [33] N. Tancogne-Dejean, O. D. Mücke, F. X. Kärtner, and A. Rubio, Ellipticity dependence of high-harmonic generation in solids originating from coupled intraband and interband dynamics, *Nat. Commun.* **8**, 745 (2017).
- [34] C. Liu, Y. Zheng, Z. Zeng, and R. Li, Driving-laser ellipticity dependence of high-order harmonic generation in graphene, *Phys. Rev. A* **97**, 063412 (2018).
- [35] X. Zhang, J. Li, Z. Zhou, S. Yue, H. Du, L. Fu, and H.-G. Luo, Ellipticity dependence transition induced by dynamical Bloch oscillations, *Phys. Rev. B* **99**, 014304 (2019).
- [36] S. A. Sato, H. Hirori, Y. Sanari, Y. Kanemitsu, and A. Rubio, High-order harmonic generation in graphene: Nonlinear coupling of intraband and interband transitions, *Phys. Rev. B* **103**, L041408 (2021).
- [37] R. Saito, G. Dresselhaus, and M. Dresselhaus, *Physical Properties of Carbon Nanotubes* (Imperial College Press, London, 1998).
- [38] J. Li, X. Zhang, S. Fu, Y. Feng, B. Hu, and H. Du, Phase invariance of the semiconductor Bloch equations, *Phys. Rev. A* **100**, 043404 (2019).
- [39] S. Jiang, H. Wei, J. Chen, C. Yu, R. Lu, and C. D. Lin, Effect of transition dipole phase on high-order-harmonic generation in solid materials, *Phys. Rev. A* **96**, 053850 (2017).
- [40] X. Song, S. Yang, R. Zuo, T. Meier, and W. Yang, Enhanced high-order harmonic generation in semiconductors by excitation with multicolor pulses, *Phys. Rev. A* **101**, 033410 (2020).
- [41] M. Baudisch, A. Marini, J. D. Cox, T. Zhu, F. Silva, S. Teichmann, M. Massicotte, F. Koppens, L. S. Levitov, F. J. García de Abajo, and J. Biegert, Ultrafast nonlinear optical response of Dirac fermions in graphene, *Nat. Commun.* **9**, 1018 (2018).
- [42] G. Vampa, C. R. McDonald, G. Orlando, D. D. Klug, P. B. Corkum, and T. Brabec, Theoretical Analysis of High-Harmonic Generation in Solids, *Phys. Rev. Lett.* **113**, 073901 (2014).
- [43] X. Song, R. Zuo, S. Yang, P. Li, T. Meier, and W. Yang, Attosecond temporal confinement of interband excitation by intraband motion, *Opt. Express* **27**, 2225 (2019).
- [44] L. Yue and M. B. Gaarde, Imperfect Recollisions in High-Harmonic Generation in Solids, *Phys. Rev. Lett.* **124**, 153204 (2020).
- [45] T. Higuchi, C. Heide, K. Ullmann, H. B. Weber, and P. Hommelhoff, Light-field-driven currents in graphene, *Nature (London)* **550**, 224 (2017).
- [46] Z. Zhai, R.-F. Yu, X.-S. Liu, and Y.-J. Yang, Enhancement of high-order harmonic emission and intense sub-50-as pulse generation, *Phys. Rev. A* **78**, 041402(R) (2008).
- [47] J.-G. Chen, Y.-J. Yang, S.-L. Zeng, and H.-Q. Liang, Generation of intense isolated sub-40-as pulses from a coherent superposition state by quantum path control in the multicycle regime, *Phys. Rev. A* **83**, 023401 (2011).
- [48] Z. Q. Li, E. A. Henriksen, Z. Jiang, Z. Hao, M. C. Martin, P. Kim, H. L. Stormer, and D. N. Basov, Dirac charge dynamics in graphene by infrared spectroscopy, *Nat. Phys.* **4**, 532 (2008).
- [49] A. K. Geim and K. S. Novoselov, The rise of graphene, *Nat. Mater.* **6**, 183 (2007).
- [50] C. Chen, V. V. Deshpande, M. Koshino, S. Lee, A. Gondarenko, A. H. MacDonald, P. Kim, and J. Hone, Modulation of mechanical resonance by chemical potential oscillation in graphene, *Nat. Phys.* **12**, 240 (2016).
- [51] V. P. Gusynin, S. G. Sharapov, and J. P. Carbotte, Magneto-optical conductivity in graphene, *J. Phys.: Condens. Matter* **19**, 026222 (2006).